www.acsami.org Research Article

Sensitive Silicon Nanowire Ultraviolet B Photodetector Induced by Leakage Mode Resonances

Jia-Yin Liu, Jun-Jie Wang, Di-Hua Lin, Jiang Wang, Can Fu, Feng-Xia Liang,* Xiang Li, Zi-Peng Gu, Di Wu, and Lin-Bao Luo*

Cite This: *ACS Appl. Mater. Interfaces* 2022, 14, 32341−32349 Read Online

ACCESS | Metrics & More | Article Recommendations | Supporting Information

Downloaded via HEFEI UNIV OF TECHNOLOGY on September 18, 2022 at 08:47:01 (UTC).
See https://pubs.acs.org/sharingguidelines for options on how to legitimately share published articles.

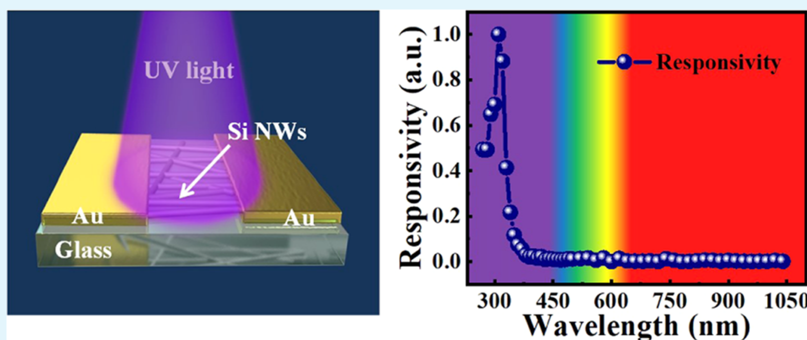

ABSTRACT: Ultraviolet photodetectors (UVPDs) have played an important role both in civil and military applications. While various studies have shown that traditional UVPDs based on wide-band-gap semiconductors (WBSs) have excellent device performances, it is, however, undeniable that the practical application of WBS-based UVPDs is largely limited by the relatively high fabrication cost. In this work, we propose a new silicon nanowire (Si NW) UVPD that is very sensitive to UVB light illumination. The Si NWs with a diameter of about 36 nm are fabricated by a metal-assisted chemical etching method. Performance analysis revealed that the Si NW device was only sensitive to UVB light and almost blind to illumination in the visible and near-infrared regions. Such abnormal spectral selectivity was associated with the leakage mode resonances (LMRs) of the small diameter, according to our theoretical simulation. Under 300 nm illumination, the responsivity, external quantum efficiency, and specific detectivity were estimated to be 10.2 AW^{-1}, 4.22×10^3%, and 2.14×10^{10} Jones, respectively, which were comparable to or even higher than those of some WBS-based UVPDs. These results illustrate that the small dimension Si NWs are potential building blocks for low-cost and high-performance UVPDs in the future.

KEYWORDS: *UV light photodetectors, silicon nanowires, leakage mode resonances, smaller diameter, finite element method*

INTRODUCTION

Ultraviolet (UV) light is electromagnetic radiation with typical wavelengths between about 10 and 400 nm. It is commonly classified as UVA (320−400 nm), UVB (280−320 nm), UVC (200−280 nm), and far UV (10−200 nm).[1] The detection of UV light has shown wide application in various civil and military fields, including environmental monitoring, flame detection, biological analysis, astronomical research, missile warning, unmanned stations, etc.[2−4] Especially, the quantitative detection of UVB light can help human beings reduce the risk of some diseases, such as skin cancer and erythema.[5,6] To date, a great number of ultraviolet photodetectors (UVPDs) with different geometries have been achieved using traditional wide-band-gap semiconductors (WBSs), such as ZnO,[7,8] TiO_2,[9] GaN,[10] etc. It has been found that in addition to the relatively high sensitivity to UV light, WBS-based UVPDs also have other advantages such as high responsivity,[11] specific detectivity,[12] well wearability,[13] and good environmental stability.[14] In spite of this, it is undeniable that WBSs are commonly grown by molecular beam epitaxy (MBE)[15] and metal−organic chemical vapor deposition (MOCVD),[16] which are characterized by complicated and critical fabrication conditions. For this reason, it is difficult to achieve mass production of these WBSs at a low cost. In addition to this, environmental friendliness is also a non-negligible problem for some WBSs.[17] As a predominant material in the semiconductor industry, silicon (Si) has been widely used in the fabrication of both integrated circuits (ICs) and photodetectors, owing to its mature preparation process and good

Received: March 14, 2022
Accepted: June 27, 2022
Published: July 7, 2022

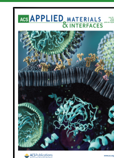

ACS Publications © 2022 American Chemical Society

https://doi.org/10.1021/acsami.2c04606
ACS Appl. Mater. Interfaces 2022, 14, 32341−32349

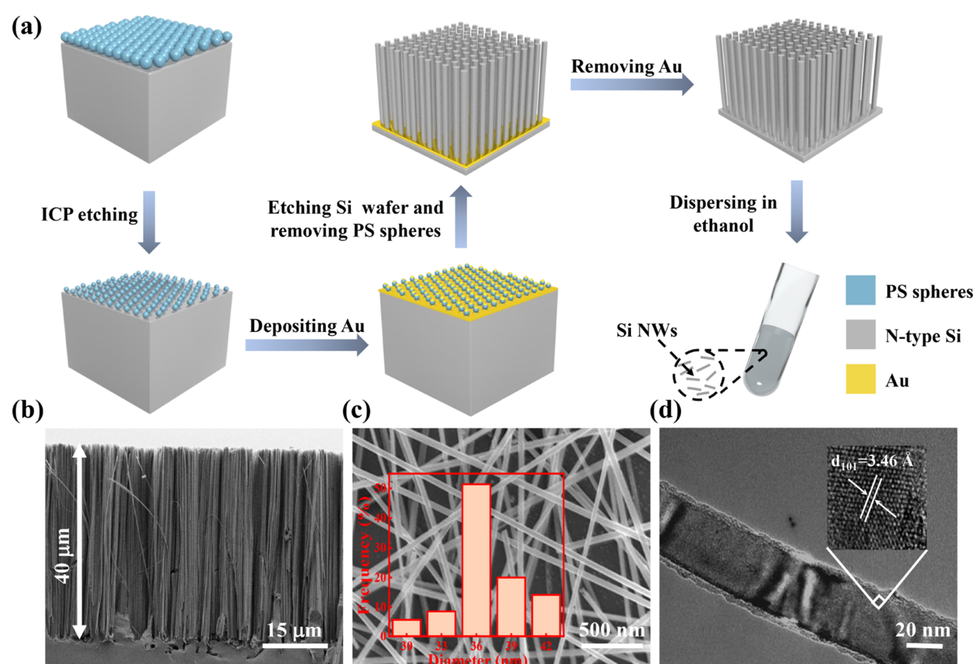

Figure 1. (a) Schematic procedure for the fabrication of small-diameter Si NWs. (b) Side-view SEM images of a Si NW array. (c) Magnified SEM images of dispersed Si NWs, and the inset shows the diameter distribution of Si NWs. (d) HRTEM image of a Si NW, and the inset shows the corresponding lattice structure.

performance.[18−20] The UV detection of Si-based photodetectors can be achieved by some approaches such as forming an ultrashallow junction and inducing an additional electric field on the Si surface.[21,22] These photodetectors usually have good device performance. In addition, UV bandpass filters that can selectively transmit UV light are often combined with Si photodetectors, which will lead to an increased fabrication cost.[23] On the other hand, some materials and light-trapping structures that can significantly enhance UV absorption are also used to improve the photoresponse of UV light.[24,25] However, these approaches are unfortunately not compatible with conventional Si manufacturing technology.

Various studies have shown that the photoabsorption of semiconductor nanowires (NWs) is quite different from that of their thin-film or bulk counterparts.[26,27] These findings are believed to be due to the leakage mode resonances (LMRs), which can be understood as optical antenna effects in one-dimensional (1D) high-refractive-index semiconductor nanostructures.[28] When the NWs are under illuminations that match leakage modes, the light trapped inside NWs will be internally reflected multiple times by the boundary.[29] It has also been reported that NWs of different diameters can enhance the photoabsorption in a specific region, and horizontal NWs tend to support transverse magnetic (TM) and transverse electric (TE) LMRs, which are determined by the diameters of NWs.[30] By this token, a device composed of semiconductor nanostructures can bring about new optoelectronic characteristics, which are quite different from the devices made of thin-film or bulk materials.

In this study, we report on the development of a small-diameter Si NW photodetector for UVB light detection. Device characterization reveals that the metal−semiconductor−metal (MSM) Si NW photodetector was highly sensitive to UV light illumination with peak sensitivity at around 310 nm but almost blind to visible and near-infrared light. Such a UVB sensitivity was related to leakage mode resonances (LMRs) of Si NWs, according to the theoretical simulations based on the finite element method (FEM). Further comparison of the device parameters finds that the responsivity of the present Si NW UVPD is comparable to or even better than those of previously reported devices. It is believed that this device composed of narrow band gap semiconductor nanostructures has potential application prospects in future UVB light detection.

EXPERIMENTAL SECTION

Material Synthesis and Device Fabrication. The Si NW was obtained by a metal-catalyzed chemical etching method. Briefly, an n-type Si wafer [resistivity: 1−10 Ω cm, (100) oriented] was ultrasonically cleaned in acetone, ethanol, and deionized water for 15 min, respectively. The clean Si substrate was treated with Ar plasma for 5 min to increase the surface hydrophilicity. Next, a single layer of polystyrene (PS) spheres (diameter: 100 nm) was loaded onto the Si wafer. Then, the diameters of PS spheres were reduced through inductively coupled plasma (ICP-601). The radio frequency (RF) power of the top electrode was set to be 140 W and that of the bottom electrode was set to be 40 W. The flow rate of O_2, the constant pressure in the chamber, and the etching time were set to be 50 standard cubic centimeters per minute (sccm), 5 m-torr, and 80 s, respectively. Afterward, a Au layer with a thickness of about 20 nm was deposited on the Si surface. During this process, the PS sphere with a reduced diameter will act as the mask layer that will lead to the formation of a continuous gold nanofilm with spherical voids in it. The above Si sample was then immersed in an etching solution [$HF:H_2O_2:H_2O$ = 4:1:5 (v/v)] for 1 h to obtain a Si NW array. After that, the PS spheres were removed with acetone, and the sample was dissolved in a mixed solution composed of I_2 and KI to etch the remaining Au catalysts. The as-etched Si NW was finally immersed in ethanol and placed in an ultrasonic cleaning machine for 15 s to disperse Si NWs in ethanol uniformly. To fabricate the device, the above suspension was dropped on a quartz glass substrate, and the ethanol solvent was evaporated after annealing at 60 °C for 10 min. Then, a mask with a channel size of 20 μm was covered on Si NWs, and a 50 nm Au film was deposited as the electrode by electron-beam evaporation.

https://doi.org/10.1021/acsami.2c04606
ACS Appl. Mater. Interfaces 2022, 14, 32341−32349

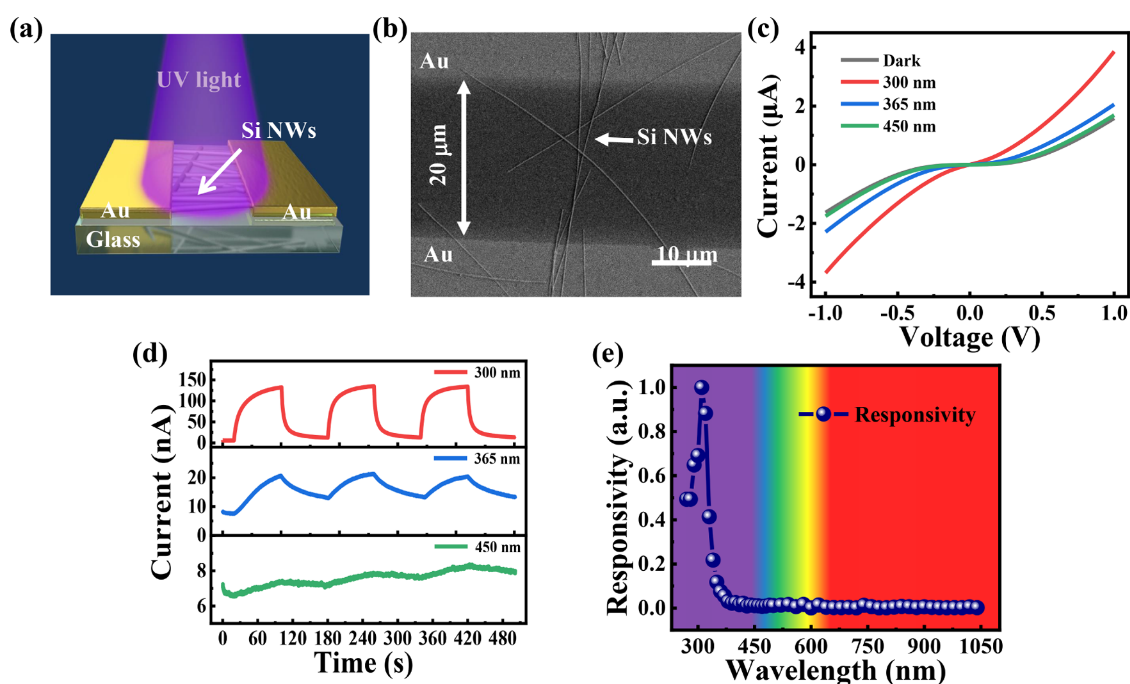

Figure 2. (a) Schematic diagram of Si NW UVPD. (b) SEM image of the device channel. (c) $I-V$ characteristics of the Si NW UVPD in the dark and under illumination at various wavelengths, and the light intensities are all set to be 2.0 mW cm^{-2}. (d) Time-dependent photoresponse under 300, 365, and 450 nm light illuminations (2.0 mW cm^{-2}) at a bias voltage of 0.1 V. (e) Normalized spectral responsivity of the Si NW UVPD.

Material Characterization and Device Analysis and Simulation. The morphologies of PS spheres and Si NWs were characterized with a scanning electron microscope (SEM, SIRION 200 FEG). The crystal structure of Si NWs was analyzed with a high-resolution transmission electron microscope (HRTEM, JEM-2100 F). The electrical measurement of our device was tested on a semiconductor parameter test system (Keithley 4200-SCS), and the photoresponse characteristics were measured using a monochromator (LE-SP-M300) and laser diodes of different wavelengths (300, 365, and 450 nm). Commercial software COMSOL Multiphysics 5.4 was used to perform all of the numerical simulations. In these simulations, the plane wave propagated along the y-axis, and the wavelength range was set from 270 to 1100 nm. A perfectly matched layer was set both at the top and the bottom of the structure to avoid nonphysical reflections of outgoing electromagnetic waves. The absorption value can be obtained by calculating the result of the incident power minus the transmitted power and reflected power. The dielectric constant of air was 1 in all simulations.

RESULTS AND DISCUSSION

In this study, smaller-diameter Si NWs were synthesized by a metal-assisted chemical etching (MCE) method.[31,32] Figure 1a illustrates the stepwise fabrication process of Si NWs. To precisely control the diameter of the Si NWs, polystyrene (PS) spheres with uniform diameter were packed on the substrate surface, as shown by the SEM image (Figure S1a). Then, the diameters of PS spheres were reduced by inductively coupled plasma (ICP) etching. These small-diameter spheres actually act as a mask for forming continuous Au thin films (Figure S1b), whose morphology is of paramount importance for forming a large-scale Si NW array with an identical diameter during the MCE process (note that the Au nanofilm can actually act as a catalyst that can direct the anisotropic etching of Si).[33] Afterward, the vertical Si NW array was obtained by immersing the above Si sample into a mixed etching solution (see the Experimental Section for more details). Finally, the Au film at the bottom part of the Si wafer and spheres were removed in two different solutions, assisted by an ultrasonic method.[34] The SEM image in Figure 1b reveals that the length of the as-etched NWs was about 40 μm. A further magnified SEM image in Figure 1c observes that Si NWs have a relatively uniform diameter (Figure 1c), with an average diameter of approximately 36 nm, according to the statistical distribution shown in the inset of Figure 1c. Figure 1d displays the HRTEM image of the Si NW, which proves that the nanostructures obtained by this method have typical single-crystal properties. What is more, there was a natural oxide layer with a thickness of around 2 nm on Si NWs, which is reasonable due to exposure to ambient conditions.[35]

An ultraviolet photodetector was then fabricated using a metal−semiconductor−metal (M−S−M) device geometry, to study the optoelectronic properties of Si NWs. Figure 2a illustrates the device structure, in which multiple Si NWs were in contact with two parallel Au electrodes, forming two back-to-back Schottky junctions. As shown by the SEM image in Figure 2b, the channel has a typical width of around 20 μm. Figure 2c,d depicts the current−voltage ($I-V$) curve of the device in the dark and under illumination at different wavelengths (300, 365, and 450 nm) with a light intensity of 2 mW cm^{-2}. It is apparent that the device is most sensitive to 300 nm light and almost blind to 450 nm light. The rejection ratio (300 nm:450 nm) is 50.3 at 0.1 V, suggesting that this device has an excellent anti-interference capability to visible light.[36] Further normalized spectral responsivity in Figure 2e shows that the peak photoresponse of this photodetector is around 310 nm illumination, and it is blind to visible and other near-infrared illuminations. This finding is completely different from previously reported silicon nanostructure-based photodetectors (the majority of the peak sensitivity is centered at 1000 nm), including conformal graphene/Si nanoholes,[37] Ti/Si NW array/Au,[38] and Cu/Si nanopyramids.[39]

https://doi.org/10.1021/acsami.2c04606
ACS Appl. Mater. Interfaces 2022, 14, 32341−32349

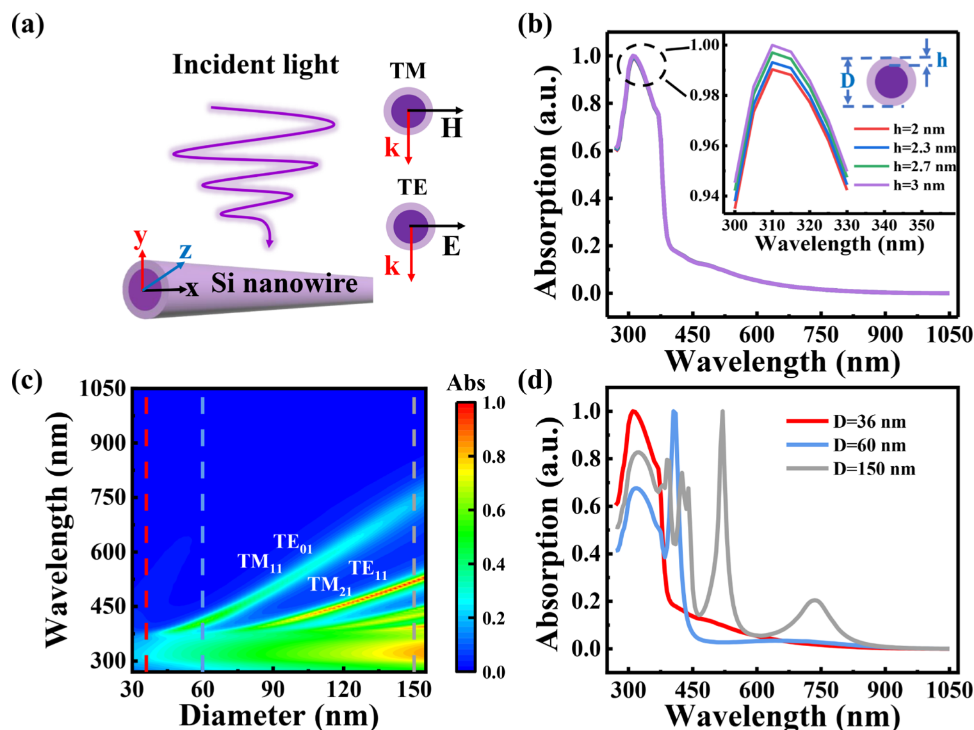

Figure 3. (a) Schematic illustration of a horizontal Si NW, and the inset illustrates TM (electric field of the light polarized parallel to the axis of the wire) and TE (electric field of the light polarized perpendicular to the axis of the wire) modes. (b) Simulations of the absorption spectrum of NWs with SiO_2 of various thicknesses, and the inset shows the cross section of NWs. (c) Contour plot of the absorption as a function of the wavelength and Si NW diameters. (d) Simulations of the absorption spectra of Si NWs with diameters of 36, 60, and 150 nm, respectively.

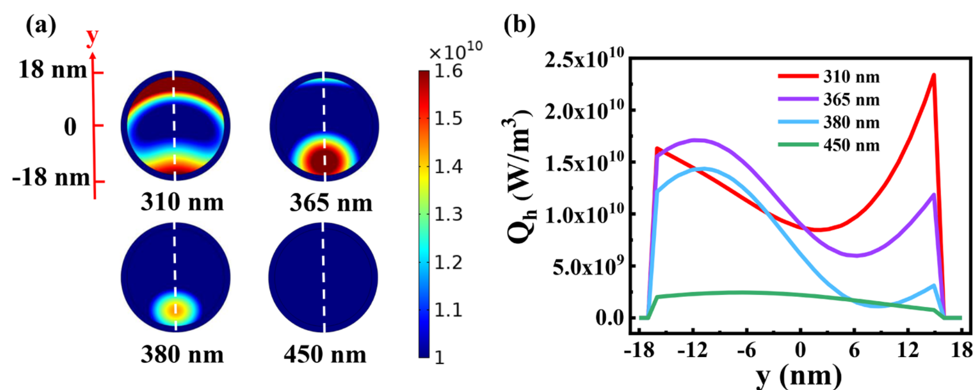

Figure 4. (a) Total power loss density plots in the *x*−*y* planes excited by illumination with wavelengths of 310, 365, 380, and 450 nm, respectively. (b) Total power loss density corresponding to the positions of the dashed lines in (a).

To shed light on the underlying reason for the unusual spectral selectivity of the present Si NW photodetector, theoretical simulations based on the FEM method were then used to study the optical properties of Si NWs. Figure 3a presents a schematic diagram of the horizontal Si NW, where the light is incident along the *y*-axis. The total diameter of NWs was set to be 36 nm (D = 36 nm) with a 2 nm thick silicon oxide layer (h = 2 nm), and the length was set to be infinite. Figure 3b reveals the optical absorption of Si NWs with different oxide layer thicknesses. It can be found that the spectral absorption of Si NWs with varied thicknesses (2, 2.3, 2.7, and 3 nm) is nearly the same, suggesting that a slight change in the silicon oxide thickness cannot change the photoabsorption of Si NWs. Figure 3c is a representative contour plot that illustrates the dependence of the photoabsorption of Si NWs on their diameter and illumination wavelength. One can clearly see that in the diameter range of 30−150 nm, the photoabsorption of Si NWs could be continuously tuned in the visible and the UV range, and as the diameter further decreases, the absorption peaks due to the TM_{21}, TE_{11}, and TM_{11}, TE_{01} LMRs will shift to shorter wavelengths. The first subscript is an azimuthal mode number indicating the effective number of wavelengths around the wire circumference, and the second one is a radial order number describing the number of radial field maxima within the nanowire, according to the solution of Maxwell's equation (see the SI).[30] As a matter of fact, such a diameter-dependent photoabsorption is understandable considering the optical antenna effect of the Si NWs: when the incident light is effectively coupled with leakage mode, the photoabsorption of NWs in a particular spectrum will be enhanced.[30] According to the solution of Maxwell's equation, it is found that as the radius

https://doi.org/10.1021/acsami.2c04606
ACS Appl. Mater. Interfaces 2022, 14, 32341−32349

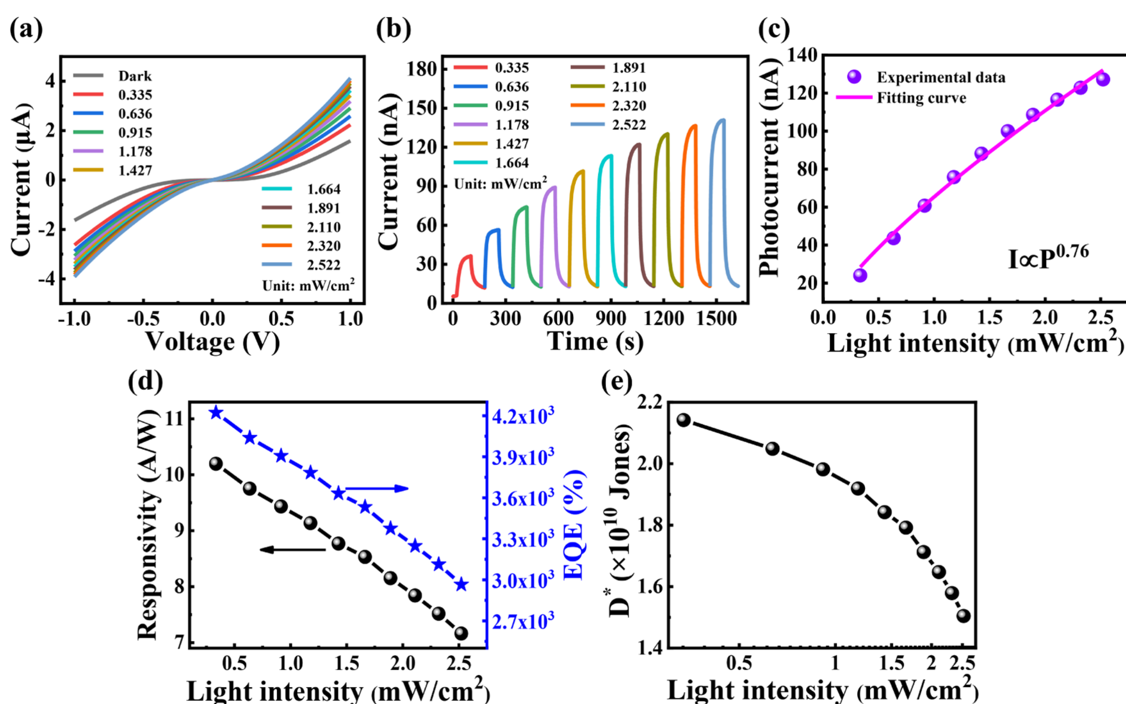

Figure 5. (a) $I-V$ curves of the device with various light intensities under 300 nm illumination. (b) Time-dependent photoresponse of the UVPD with different intensities under 300 nm light at 0.1 V. (c) Photocurrent of the photodetector as a function of incident light intensity. (d) Responsivity and EQE under 300 nm illumination with different light intensities. (e) Specific detectivity (D^*) with various light intensities.

of the NW reduces, the wavelength corresponding to the specific leakage mode decreases, which results in a blue shift of the absorption peak (more details are available in the SI). Figure 3d shows the corresponding absorption spectra of Si NWs with diameters of 36, 60, and 150 nm (for the sake of consistency, three kinds of Si NWs are all core−shell nanostructures that have a uniform sheath of 2 nm SiO_2 nanofilm), respectively. An obvious absorption peak attributable to LMRs can be observed at wavelengths of 310, 405, 520, 735 nm, etc. From the electric field distribution shown in Figure S2, it can be seen that the absorption peak at 520 nm of 150 nm Si NWs is related to TM_{21} and TE_{11} LMRs, while the absorption peak at 735 nm is related to TM_{11} and TE_{01} LMRs, which is consistent with the previous study.[40] Although the details of LMRs for the 36 nm Si NW are still unclear to us, it, however, can directly lead to the shift of peak absorption to 310 nm, which is of paramount importance to UVB detection.

To further study the enhanced absorption properties of Si NWs, other theoretical simulations were also performed. Figure 4a shows the total power loss density distributions of a 36 nm diameter Si NW under 310, 365, 380, and 450 nm illumination, respectively. One can easily see that there is almost no power loss in the silicon dioxide layer. More importantly, the strongest total power loss of Si NWs is found when the incident wavelength is 310 nm light. In contrast, there is almost no power loss under 450 nm illumination. Figure 4b further depicts the total power loss density (Q_h) corresponding to the dashed line in Figure 4a. Since the power loss is mainly caused by the intrinsic absorption, the value of Q_h can directly reflect the strength of Si NW absorption.[41] It can be found that the power loss inside the NW declined as the illumination shifted to longer wavelengths. In addition, there is apparent power loss both at the top and bottom of NWs for the short wavelength of illumination, especially when the NW was under 310 nm illumination, suggesting that 310 nm light illumination can be easily absorbed by the Si NWs, and therefore can be easily detected.[42]

Further study reveals that the photocurrent of the Si NW is dependent on the light intensity as well. Figure 5a compares the $I-V$ curves of the Si NW UVPD under 300 nm illumination with different light intensities. Obviously, with increasing light intensity, the photocurrents increase accordingly, due to more photogenerated carriers in Si NWs. Specifically, when the light intensity increased from 0.335 to 2.522 mW cm^{-2}, the photocurrent at 0.1 V bias could be improved from 36.12 to 140.64 nA. The relationship between the photocurrent and light intensity can be further quantitatively described by a power law: $I_{ph} \propto P^{\theta}$. I_{ph} is the net photocurrent ($I_{ph} = I_{light} - I_{dark}$), P is the light intensity, and θ is the exponent of photoresponse, which reflects the recombination activity of photogenerated carriers,[43] and the value of θ in this study is 0.76, indicative of the recombination loss in our device under a high light intensity.[44] To quantitatively study the performance of Si NW UVPD, some key performance parameters like responsivity (R), external quantum efficiency (EQE), and specific detectivity (D^*) were computed by the following formulas[45−47]

$$R = \frac{I_{light} - I_{dark}}{PS} \tag{1}$$

$$\mathrm{EQE} = \frac{hcR}{q\lambda} \tag{2}$$

$$D^* = \frac{(S\Delta f)^{1/2}}{\mathrm{NEP}} \tag{3}$$

$$\mathrm{NEP} = \frac{\overline{i_n^2}^{1/2}}{R} \tag{4}$$

https://doi.org/10.1021/acsami.2c04606
ACS Appl. Mater. Interfaces 2022, 14, 32341−32349

Table 1. Comparison of the Device Parameters of Our Photodetector and Other WBS-Based UV Photodetectors

device structure	wavelength [nm]	bias [V]	R [AW^{-1}]	D^* [Jones]	ref
Au-Si NWs-Au	300	0.1	10.2	2.14×10^{10}	this work
Au-TiO_2 film-Au	310	5	3.27×10^{-3}		55
Pt-$Mg_{0.05}Zn_{0.95}O$ film-Pt	315	7	0.4	1.8×10^{10}	56
Au-GaN film-Au	325	5	0.34	1.24×10^{9}	57
Au-SnO_2 film-Au	290	5	2.84×10^{-2}		58
graphene-ZnS nanobelts-graphene	300	1	1.9×10^{3}		54
Ni_2Si/6H-SiC film/Ni	320	0	0.07		59
Au/AlGaN film/Au	304	−20	0.202		60
Au/$Ga_{0.3}Zn_{0.7}O$ film/Au	310	5	0.57	4.5×10^{9}	61

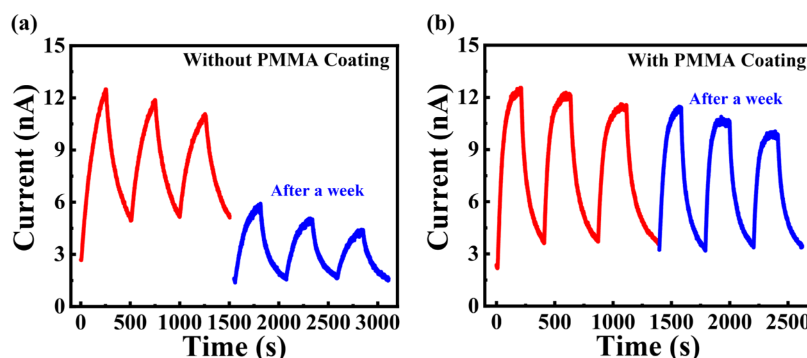

Figure 6. Comparison of the photoresponse of the device without (a) and with (b) PMMA coating before and after storage in air for a week, respectively, and the light intensity is set to be 0.5 mW cm^{-2}.

where P is the power density of the incident light, S is the effective illumination area (7.04×10^{-6} cm^2), h is Planck's constant, c is the speed of light, and q is the value of the electron charge. Δf is the bandwidth equivalent power, $\overline{i_n^2}^{1/2}$ is the root-mean-square value of the noise current in the dark, and NEP denotes the noise equivalent power. As shown in Figure S3, Fourier transformation was performed to the dark current, and the value of NEP was calculated to be 2.40×10^{-13} $WHz^{-1/2}$. According to the above equations, the values of R, EQE, and D^* were estimated to be 10.2 AW^{-1}, 4.22×10^3%, and 2.14×10^{10} Jones, respectively. Further statistical distribution of 10 similar devices shows that the average values of R, EQE, and D^* of devices were estimated to be 9.77 AW^{-1}, 4.04×10^3%, and 1.90×10^{10} Jones, respectively. In addition, the corresponding standard deviation of these parameters were around 3.19 AW^{-1}, 1.32×10^3%, and 6.61×10^9 Jones (Figure S4), respectively. It is found in Figure 5d,e that R, EQE, and D^* will decline with the increase of light intensity. This can be explained as follows: under weak light illumination, the number of photogenerated carriers was so small that all of these carriers could be separated effectively by the built-in electric field. However, with the increase in light intensity, more carriers were generated, which led to a higher degree of recombination. Thereby, only a small fraction of carriers could be effectively separated by the built-in electric field.[48,49] As a result, the values of R, EQE, and D^* all decreased under a high light intensity. In addition, the rise/fall time of the Au/Si NWs/Au UVPD is estimated to be 23.3:20.9 s, which is relatively slower than that of previously reported M−S−M devices (Figure S5).[50,51] This may be due to the high-density surface states of small-diameter Si NWs.[52,53] Table 1 compares the key device performance parameters (R and D^*) of our device and other WBS-based UVPDs. The R of our UVPD is poorer than that of the UVPD based on ZnS nanobelts.[54] However, the R and D^* in this work are better than those of other UVPDs composed of conventional WBS materials including the TiO_2 film,[55] $Mg_{0.05}Zn_{0.95}O$ film,[56] GaN film,[57] SnO_2 film,[58] 6H-SiC film,[59] AlGaN film,[60] and $Ga_{0.3}Zn_{0.7}O$ film,[61] respectively.

Lastly, it should be noted that while the stability of the bulk Si wafer is very good in comparison with other semiconductor materials, the present Si NW photodetector, however, displays a relatively poor ambient stability. Figure 6a compares the stability of our device after storage in air for a week, from which, the photocurrent was found to reduce by 50%. Such poor ambient stability is probably due to the relatively large surface area that is relatively active and can react with air, gas, or humid molecules after long-term exposure. As a matter of fact, such poor stability could be improved by coating PMMA on the surface. As Figure 6b depicted, under the same conditions, there was almost no decrease in the photocurrent of the device coated by PMMA.

CONCLUSIONS

In summary, we have reported an MSM horizontal UV light photodetector, in which the diameter of Si NWs is about 36 nm. This device is sensitive to UVB light but is almost blind to light in the visible and near-infrared regions. According to the theoretical simulation based on FEM, this special UVB photoresponse is associated with the relatively strong light absorption in the UVB region, which can be attributed to leakage mode resonances of the small diameter of the Si NWs. Under 300 nm illumination at 0.1 V bias, the R, EQE, and D^* of this UVB are estimated to be 10.2 AW^{-1}, 4.22×10^3%, and 2.14×10^{10} Jones, respectively, which are comparable to or even better than other UVPDs based on traditional WBSs. These relatively good device performances indicate that small

https://doi.org/10.1021/acsami.2c04606
ACS Appl. Mater. Interfaces 2022, 14, 32341−32349

dimension Si NWs are promising building blocks for the assembly of UV optoelectronic devices in the future.

ASSOCIATED CONTENT

Supporting Information

The Supporting Information is available free of charge at https://pubs.acs.org/doi/10.1021/acsami.2c04606.

> SEM images of PS spheres; electric field distribution of 150 nm diameter Si NWs under illumination with different wavelengths; solution of leaky modes; analysis of noise spectral density of the device with the dark current noise using Fourier transform; distribution of R, EQE, and D^* for 10 Au/Si NWs/Au photodetectors; a single normalized cycle of the device; and the method for calculating the effective area of the photodetector. (PDF)

AUTHOR INFORMATION

Corresponding Authors

Feng-Xia Liang − *School of Microelectronics, Hefei University of Technology, Hefei 230009, China*; orcid.org/0000-0002-8237-3534; Email: fxliang@hfut.edu.cn

Lin-Bao Luo − *School of Microelectronics, Hefei University of Technology, Hefei 230009, China*; Email: luolb@hfut.edu.cn

Authors

Jia-Yin Liu − *School of Microelectronics, Hefei University of Technology, Hefei 230009, China*

Jun-Jie Wang − *School of Microelectronics, Hefei University of Technology, Hefei 230009, China*

Di-Hua Lin − *School of Physics, Hefei University of Technology, Hefei 230009, China*

Jiang Wang − *School of Microelectronics, Hefei University of Technology, Hefei 230009, China*

Can Fu − *School of Microelectronics, Hefei University of Technology, Hefei 230009, China*

Xiang Li − *School of Microelectronics, Hefei University of Technology, Hefei 230009, China*

Zi-Peng Gu − *School of Microelectronics, Hefei University of Technology, Hefei 230009, China*

Di Wu − *Key Laboratory of Materials Physics of Ministry of Education, Department of Physics and Engineering, Zhengzhou University, Zhengzhou 450052, China*; orcid.org/0000-0003-3266-0612

Complete contact information is available at: https://pubs.acs.org/10.1021/acsami.2c04606

Author Contributions

J.Y.L. and J.J.W. prepared the device, tested, and analyzed the performance, simulated optical properties, and wrote the manuscript; L.B.L. and F.X.L. provided the idea, analyzed data, and wrote the manuscript; D.H.L., J.W., and C.F. helped with the synthesis of materials and data processing; and X.L., Z.P.G., and D.W. assisted in literature research and the study of material properties. All authors discussed the results and commented on the manuscript.

Notes

The authors declare no competing financial interest.

ACKNOWLEDGMENTS

This work was supported by the National Natural Science Foundation of China (NSFC, No. 62074048), the Key Research and Development Plan of Anhui Province (2022f04020007), and the Fundamental Research Funds for the Central Universities (JZ2018HGXC0001, JZ2018HGPB0275, and PA2020GDKC0014).

REFERENCES

(1) Peng, L.; Hu, L.; Fang, X. Low-Dimensional Nanostructure Ultraviolet Photodetectors. *Adv. Mater.* **2013**, *25*, 5321−5328.

(2) Zou, T.; Liu, X.; Qiu, R.; Wang, Y.; Huang, S.; Liu, C.; Dai, Q.; Zhou, H. Enhanced UV-C Detection of Perovskite Photodetector Arrays via Inorganic $CsPbBr_3$ Quantum Dot Down-Conversion Layer. *Adv. Opt. Mater.* **2019**, *7*, No. 1801812.

(3) Xiao, H.; Liang, T.; Xu, M. Growth of Ultraflat PbI_2 Nanoflakes by Solvent Evaporation Suppression for High-Performance UV Photodetectors. *Small* **2019**, *15*, No. 1901767.

(4) Zhou, X.; Zhang, Q.; Gan, L.; Li, X.; Li, H.; Zhang, Y.; Golberg, D.; Zhai, T. High-Performance Solar-Blind Deep Ultraviolet Photodetector Based on Individual Single-Crystalline Zn_2GeO_4 Nanowire. *Adv. Funct. Mater.* **2016**, *26*, 704−712.

(5) Nasiri, N.; Bo, R.; Hung, T. F.; Roy, V. A. L.; Fu, L.; Tricoli, A. Tunable Band-Selective UV-Photodetectors by 3D Self-Assembly of Heterogeneous Nanoparticle Networks. *Adv. Funct. Mater.* **2016**, *26*, 7359−7366.

(6) Xu, X.; Chen, J.; Cai, S.; Long, Z.; Zhang, Y.; Su, L.; He, S.; Tang, C.; Liu, P.; Peng, H.; Fang, X. A Real-Time Wearable UV-Radiation Monitor Based on a High-Performance p-CuZnS/n-TiO_2 Photodetector. *Adv. Mater.* **2018**, *30*, No. 1803165.

(7) Meng, L.; Li, G.; Tian, X.; Bai, S.; Xu, Q.; Jia, X.; Cui, X.; Qin, Y.; Wu, W. Ultrasensitive Fiber-Based ZnO Nanowire Network Ultraviolet Photodetector Enabled by the Synergism between Interface and Surface Gating Effects. *ACS Appl. Mater. Interfaces* **2020**, *12*, 1054−1060.

(8) Guo, N.; Xiao, L.; Gong, F.; Luo, M.; Wang, F.; Jia, Y.; Chang, H.; Liu, J.; Li, Q.; Wu, Y.; Wang, Y.; Shan, C.; Xu, Y.; Zhou, P.; Hu, W. Light-Driven WSe_2-ZnO Junction Field-Effect Transistors for High-Performance Photodetection. *Adv. Sci.* **2020**, *7*, No. 1901637.

(9) Fang, H.; Zheng, C.; Wu, L.; Li, Y.; Cai, J.; Hu, M.; Fang, X.; Ma, R.; Wang, Q.; Wang, H. Solution-Processed Self-Powered Transparent Ultraviolet Photodetectors with Ultrafast Response Speed for High-Performance Communication System. *Adv. Funct. Mater.* **2019**, *29*, No. 1809013.

(10) Li, J.; Xi, X.; Li, X.; Lin, S.; Ma, Z.; Xiu, H.; Zhao, L. Ultra-High and Fast Ultraviolet Response Photodetectors Based on Lateral Porous GaN/Ag Nanowires Composite Nanostructure. *Adv. Opt. Mater.* **2020**, *8*, No. 1902162.

(11) Wang, D.; Huang, C.; Liu, X.; Zhang, H.; Yu, H.; Fang, S.; Ooi, B. S.; Mi, Z.; He, J. H.; Sun, H. Highly Uniform, Self-Assembled AlGaN Nanowires for Self-Powered Solar-Blind Photodetector with Fast-Response Speed and High Responsivity. *Adv. Opt. Mater.* **2020**, *9*, No. 2000893.

(12) Guo, D.; Su, Y.; Shi, H.; Li, P.; Zhao, N.; Ye, J.; Wang, S.; Liu, A.; Chen, Z.; Li, C.; Tang, W. Self-Powered Ultraviolet Photodetector with Superhigh Photoresponsivity (3.05 A/W) Based on the GaN/Sn:Ga_2O_3 pn Junction. *ACS Nano* **2018**, *12*, 12827−12835.

(13) Zhang, Y.; Li, S.; Li, Z.; Liu, H.; Liu, X.; Chen, J.; Fang, X. High-Performance Two-Dimensional Perovskite $Ca_2Nb_3O_{10}$ UV Photodetectors. *Nano Lett.* **2021**, *21*, 382−388.

(14) Shao, D.; Zhu, W.; Liu, X.; Li, M.; Chen, J.; Sun, Y. Y.; Xin, G.; Lian, J.; Sawyer, S.; Ultrasensitive, U. V. Photodetector Based on Interfacial Charge-Controlled Inorganic Perovskite-Polymer Hybrid Structure. *ACS Appl. Mater. Interfaces* **2020**, *12*, 43106−43114.

(15) Wang, X.; Liu, K.; Chen, X.; Li, B.; Jiang, M.; Zhang, Z.; Zhao, H.; Shen, D. Highly Wavelength-Selective Enhancement of Responsivity in Ag Nanoparticle-Modified ZnO UV Photodetector. *ACS Appl. Mater. Interfaces* **2017**, *9*, 5574−5579.

(16) Peng, M.; Liu, Y.; Yu, A.; Zhang, Y.; Liu, C.; Liu, J.; Wu, W.; Zhang, K.; Shi, X.; Kou, J.; Zhai, J.; Wang, Z. L. Flexible Self-Powered GaN Ultraviolet Photoswitch with Piezo-Phototronic Effect Enhanced On/Off Ratio. *ACS Nano* **2016**, *10*, 1572−1579.
(17) Chen, Z.; Li, C.; Zhumekenov, A. A.; Zheng, X.; Yang, C.; Yang, H.; He, Y.; Turedi, B.; Mohammed, O. F.; Shen, L.; Bakr, O. M. Solution-Processed Visible-Blind Ultraviolet Photodetectors with Nanosecond Response Time and High Detectivity. *Adv. Opt. Mater.* **2019**, *7*, No. 1900506.
(18) Chang, K. E.; Yoo, T. J.; Kim, C.; Kim, Y. J.; Lee, S. K.; Kim, S. Y.; Heo, S.; Kwon, M. G.; Lee, B. H. Gate-Controlled Graphene-Silicon Schottky Junction Photodetector. *Small* **2018**, *14*, No. 1801182.
(19) Zhang, A.; Kim, H.; Cheng, J.; Lo, Y. H. Ultrahigh Responsivity Visible and Infrared Detection Using Silicon Nanowire Phototransistors. *Nano Lett.* **2010**, *10*, 2117−2120.
(20) Liu, W.; Guo, H.; Li, W.; Wan, X.; Bodepudi, S. C.; Shehzad, K.; Xu, Y. Light-Induced Negative Differential Resistance in Gate-Controlled Graphene-Silicon Photodiode. *Appl. Phys. Lett.* **2018**, *112*, No. 201109.
(21) Shi, L.; Nihtianov, S. Comparative Study of Silicon-Based Ultraviolet Photodetectors. *IEEE Sens. J.* **2012**, *12*, 2453−2459.
(22) Wan, X.; Xu, Y.; Guo, H.; Shehzad, K.; Ali, A.; Liu, Y.; Yang, J.; Dai, D.; Lin, C.-T.; Liu, L.; Cheng, H.-C.; Wang, F.; Wang, X.; Lu, H.; Hu, W.; Pi, X.; Dan, Y.; Luo, J.; Hasan, T.; Duan, X.; Li, X.; Xu, J.; Yang, D.; Ren, T.; Yu, B. A Self-Powered High-Performance Graphene/Silicon Ultraviolet Photodetector with Ultra-Shallow Junction: Breaking the Limit of Silicon? *npj 2D Mater. Appl.* **2017**, *1*, No. 4.
(23) Li, W.-D.; Chou, S. Y. Solar-Blind Deep-UV Band-Pass Filter (250-350 nm) Consisting of A Metal Nano-Grid Fabricated by Nanoimprint Lithography. *Opt. Express* **2010**, *18*, 931−937.
(24) Sheng, X.; Yu, C.; Malyarchuk, V.; Lee, Y.-H.; Kim, S.; Kim, T.; Shen, L.; Horng, C.; Lutz, J.; Giebink, N. C.; Park, J.; Rogers, J. A. Silicon-Based Visible-Blind Ultraviolet Detection and Imaging Using Down-Shifting Luminophores. *Adv. Opt. Mater.* **2014**, *2*, 314−319.
(25) Maiti, R.; Mukherjee, S.; Dey, T.; Ray, S. K. Solution Processed Highly Responsive UV Photodetectors from Carbon Nanodot/Silicon Heterojunctions. *ACS Appl. Nano Mater.* **2019**, *2*, 3971−3976.
(26) Das, K.; Samanta, S.; Kumar, P.; Narayan, K. S.; Raychaudhuri, A. K. Fabrication of Single Si Nanowire Metal−Semiconductor−Metal Device for Photodetection. *IEEE T. Electron Dev.* **2014**, *61*, 1444−1450.
(27) Hu, L.; Chen, G. Analysis of Optical Absorption in Silicon Nanowire Arrays for Photovoltaic Applications. *Nano Lett.* **2007**, *7*, 3249−3252.
(28) Seo, K.; Wober, M.; Steinvurzel, P.; Schonbrun, E.; Dan, Y.; Ellenbogen, T.; Crozier, K. B. Multicolored Vertical Silicon Nanowires. *Nano Lett.* **2011**, *11*, 1851−1856.
(29) Cao, L.; Fan, P.; Vasudev, A. P.; White, J. S.; Yu, Z.; Cai, W.; Schuller, J. A.; Fan, S.; Brongersma, M. L. Semiconductor Nanowire Optical Antenna Solar Absorbers. *Nano Lett.* **2010**, *10*, 439−445.
(30) Cao, L.; White, J. S.; Park, J. S.; Schuller, J. A.; Clemens, B. M.; Brongersma, M. L. Engineering Light Absorption in Semiconductor Nanowire Devices. *Nat. Mater.* **2009**, *8*, 643−647.
(31) D'Ortenzi, L.; Monsu, R.; Cara, E.; Fretto, M.; Kara, S.; Rezvani, S. J.; Boarino, L. Electrical Contacts on Silicon Nanowires Produced by Metal-Assisted Etching: A Comparative Approach. *Nanoscale Res. Lett.* **2016**, *11*, No. 468.
(32) Huang, Z.; Fang, H.; Zhu, J. Fabrication of Silicon Nanowire Arrays with Controlled Diameter, Length, and Density. *Adv. Mater.* **2007**, *19*, 744−748.
(33) Katiyar, A. K.; Sinha, A. K.; Manna, S.; Ray, S. K. Fabrication of Si/ZnS Radial Nanowire Heterojunction Arrays for White Light Emitting Devices on Si Substrates. *ACS Appl. Mater. Interfaces* **2014**, *6*, 15007−15014.
(34) Mulazimoglu, E.; Coskun, S.; Gunoven, M.; Butun, B.; Ozbay, E.; Turan, R.; Unalan, H. E. Silicon Nanowire Network Metal-Semiconductor-Metal Photodetectors. *Appl. Phys. Lett.* **2013**, *103*, No. 083114.
(35) Seo, K.-i.; Sharma, S.; Yasseri, A. A.; Stewart, D. R.; Kamins, T. I. Surface Charge Density of Unpassivated and Passivated Metal-Catalyzed Silicon Nanowires. *Electrochem. Solid St.* **2006**, *9*, No. G69.
(36) Ali, A.; Shehzad, K.; Guo, H. W.; Wang, Z.; Wang, P.; Qadir, A.; Hu, W. D.; Ren, T. L.; Yu, B.; Xu, Y. In *High-Performance, Flexible Graphene/Ultra-Thin Silicon Ultra-Violet Image Sensor*, IEEE International Electron Devices Meeting (IEDM), IEEE, 2017; pp 8.6.1−8.6.4, DOI: 10.1109/IEDM.2017.8268354.
(37) Yang, J.; Tang, L.; Luo, W.; Shen, J.; Zhou, D.; Feng, S.; Wei, X.; Shi, H. Light Trapping in Conformal Graphene/Silicon Nanoholes for High-Performance Photodetectors. *ACS Appl. Mater. Interfaces* **2019**, *11*, 30421−30429.
(38) Nusir, A. I.; Bauman, S. J.; Marie, M. S.; Herzog, J. B.; Manasreh, M. O. Silicon Nanowires to Enhance the Performance of Self-Powered Near-Infrared Photodetectors with Asymmetrical Schottky Contacts. *Appl. Phys. Lett.* **2017**, *111*, No. 171103.
(39) Mei, C.; Zou, J.; Huang, X.; Zou, B.; Zhou, P.; Gan, Z.; Hu, J.; Zhang, Q.; Wang, H. High Sensitive Position-Dependent Photodetection Observed in Cu-Covered Si Nanopyramids. *Nanotechnology* **2018**, *29*, No. 205203.
(40) Fountaine, K. T.; Whitney, W. S.; Atwater, H. A. Resonant Absorption in Semiconductor Nanowires and Nanowire Arrays: Relating Leaky Waveguide Modes to Bloch Photonic Crystal Modes. *J. Appl. Phys.* **2014**, *116*, No. 153106.
(41) Lin, C.; Povinelli, M. L. Optimal Design of Aperiodic, Vertical Silicon Nanowire Structures for Photovoltaics. *Opt. Express* **2011**, *19*, A1148−A1154.
(42) Wang, J. J.; Fu, C.; Cheng, H. Y.; Tong, X. W.; Zhang, Z. X.; Wu, D.; Chen, L. M.; Liang, F. X.; Luo, L. B. Leaky Mode Resonance-Induced Sensitive Ultraviolet Photodetector Composed of Graphene/Small Diameter Silicon Nanowire Array Heterojunctions. *ACS Nano* **2021**, *15*, 16729−16737.
(43) Xie, C.; Lu, X.; Liang, Y.; Chen, H.; Wang, L.; Wu, C.; Wu, D.; Yang, W.; Luo, L. Patterned Growth of β-Ga_2O_3 Thin Films for Solar-Blind Deep-Ultraviolet Photodetectors Array and Optical Imaging Application. *J. Mater. Sci. Technol.* **2021**, *72*, 189−196.
(44) Wang, B.; Zhang, C.; Zeng, B.; Wu, C. Y.; Xie, C.; Wu, D.; Zhou, Y. X.; Luo, L. B. Fabrication of Addressable Perovskite Film Arrays for High-Performance Photodetection and Real-Time Image Sensing Application. *J. Phys. Chem. Lett.* **2021**, *12*, 2930−2936.
(45) Kang, C. H.; Dursun, I.; Liu, G.; Sinatra, L.; Sun, X.; Kong, M.; Pan, J.; Maity, P.; Ooi, E. N.; Ng, T. K.; Mohammed, O. F.; Bakr, O. M.; Ooi, B. S. High-Speed Colour-Converting Photodetector with All-Inorganic $CsPbBr_3$ Perovskite Nanocrystals for Ultraviolet Light Communication. *Light Sci. Appl.* **2019**, *8*, No. 94.
(46) Li, Y.; Shi, Z.; Liang, W.; Wang, L.; Li, S.; Zhang, F.; Ma, Z.; Wang, Y.; Tian, Y.; Wu, D.; Li, X.; Zhang, Y.; Shan, C.; Fang, X. Highly Stable and Spectrum-Selective Ultraviolet Photodetectors Based on Lead-Free Copper-Based Perovskites. *Mater. Horiz.* **2020**, *7*, 530−540.
(47) Wang, F.; Luo, P.; Zhang, Y.; Huang, Y.; Zhang, Q.; Li, Y.; Zhai, T. Band Structure Engineered Tunneling Heterostructures for High-Performance Visible and Near-Infrared Photodetection. *Sci. China Mater.* **2020**, *63*, 1537−1547.
(48) Wu, E.; Wu, D.; Jia, C.; Wang, Y.; Yuan, H.; Zeng, L.; Xu, T.; Shi, Z.; Tian, Y.; Li, X. In Situ Fabrication of 2D WS_2/Si Type-II Heterojunction for Self-Powered Broadband Photodetector with Response up to Mid-Infrared. *ACS Photonics* **2019**, *6*, 565−572.
(49) Yang, J.; Kang, W.; Liu, Z.; Pi, M.; Luo, L. B.; Li, C.; Lin, H.; Luo, Z.; Du, J.; Zhou, M.; Tang, X. High-Performance Deep Ultraviolet Photodetector Based on a One-Dimensional Lead-Free Halide Perovskite $CsCu_2I_3$ Film with High Stability. *J. Phys. Chem. Lett.* **2020**, *11*, 6880−6886.
(50) Wang, Y.; Gan, L.; Chen, J.; Yang, R.; Zhai, T. Achieving Highly Uniform Two-Dimensional PbI_2 Flakes for Photodetectors via Space Confined Physical Vapor Deposition. *Sci. Bull.* **2017**, *62*, 1654−1662.

(51) Cai, Y.; Shen, S.; Zhu, C.; Zhao, X.; Bai, J.; Wang, T. Nonpolar (1120) GaN Metal-Semiconductor-Metal Photodetectors with Superior Performance on Silicon. *ACS Appl. Mater. Interfaces* **2020**, *12*, 25031−25036.
(52) Jie, J.; Zhang, W.; Peng, K.; Yuan, G.; Lee, C. S.; Lee, S. T. Surface-Dominated Transport Properties of Silicon Nanowires. *Adv. Funct. Mater.* **2008**, *18*, 3251−3257.
(53) Yan, C.; Wang, J.; Wang, X.; Kang, W.; Cui, M.; Foo, C. Y.; Lee, P. S. An Intrinsically Stretchable Nanowire Photodetector with A Fully Embedded Structure. *Adv. Mater.* **2014**, *26*, 943−950.
(54) Kim, Y.; Kim, S. J.; Cho, S. P.; Hong, B. H.; Jang, D. J. High-Performance Ultraviolet Photodetectors Based on Solution-Grown ZnS Nanobelts Sandwiched between Graphene Layers. *Sci. Rep.* **2015**, *5*, No. 12345.
(55) Huang, H.; Xie, Y.; Zhang, Z.; Zhang, F.; Xu, Q.; Wu, Z. Growth and Fabrication of Sputtered TiO_2 Based Ultraviolet Detectors. *Appl. Surf. Sci.* **2014**, *293*, 248−254.
(56) Bhardwaj, R.; Sharma, P.; Singh, R.; Gupta, M.; Mukherjee, S. High Responsivity $Mg_xZn_{1-x}O$ Based Ultraviolet Photodetector Fabricated by Dual Ion Beam Sputtering. *IEEE Sens. J.* **2018**, *18*, 2744−2750.
(57) Gundimeda, A.; Krishna, S.; Aggarwal, N.; Sharma, A.; Sharma, N. D.; Maurya, K. K.; Husale, S.; Gupta, G. Fabrication of Non-Polar GaN Based Highly Responsive and Fast UV Photodetector. *Appl. Phys. Lett.* **2017**, *110*, No. 103507.
(58) Zheng, Q.; Zheng, Y.; Huang, J.; Li, H. High Performance UV-B Photodetector Based on Highly (200)-Oriented SnO_2 Film with A Hydrophobic PTFE Passivation Layer. *IEEE Sens. J.* **2021**, *21*, 9825−9832.
(59) Sciuto, A.; Mazzillo, M. C.; Di Franco, S.; Mannino, G.; Badala, P.; Renna, L.; Caruso, C. UV-A Sensor Based on 6H-SiC Schottky Photodiode. *IEEE Photonics J.* **2017**, *9*, 1−10.
(60) Hou, Q.; You, H.; Cai, Q.; Guo, H.; Shao, P.; Pan, D.; Yu, L.; Chen, D.; Lu, H.; Zhang, R.; Zheng, Y. A High Quantum Efficiency Narrow-Band UV-B AlGaN p-i-n Photodiode with Polarization Assistance. *IEEE Photonics J.* **2021**, *13*, 1−8.
(61) Liu, H.-Y.; Liu, G.-J. Investigation of Bandgap Engineering of Gallium Zinc Oxide-Based Ultraviolet Photodetector by Mist Atmospheric Pressure Chemical Vapor Deposition. *IEEE T. Electron Dev.* **2019**, *66*, 2256−2262.

Recommended by ACS

Broadband GaAsSb Nanowire Array Photodetectors for Filter-Free Multispectral Imaging

Ziyuan Li, Lan Fu, *et al.*
AUGUST 23, 2021
NANO LETTERS

Nanolayered Wavelength-Selective Narrowband Thermal Emitters for Solar Thermophotovoltaics

Qingyuan Wang, Kunji Chen, *et al.*
SEPTEMBER 13, 2022
ACS APPLIED NANO MATERIALS

Single-Nanowire Thermo-Optic Modulator Based on a Varshni Shift

Zhangxing Shi, Limin Tong, *et al.*
AUGUST 03, 2020
ACS PHOTONICS

GaN Nanowire/Nb-Doped MoS_2 Nanoflake Heterostructures for Fast UV–Visible Photodetectors

Xin Tang, Guoqiang Li, *et al.*
MARCH 10, 2022
ACS APPLIED NANO MATERIALS

Get More Suggestions >

https://doi.org/10.1021/acsami.2c04606
ACS Appl. Mater. Interfaces 2022, 14, 32341−32349